Hydrogen-deuterium exchange mass spectrometry of Mtr4 with diverse RNAs reveals substrate-dependent dynamics and interfaces in the arch

Naifu Zhang [1,†], Keith J. Olsen [2,†], Darby Ball [1], Sean J. Johnson [2,*] and Sheena D'Arcy [1,*]

[1]Department of Chemistry and Biochemistry, The University of Texas at Dallas, Richardson, TX75080, USA and
[2]Department of Chemistry and Biochemistry, Utah State University, Logan, UT 84322, USA

ABSTRACT

Mtr4 is a eukaryotic RNA helicase required for RNA decay by the nuclear exosome. Previous studies have shown how RNA en route to the exosome threads through the highly conserved helicase core of Mtr4. Mtr4 also contains an arch domain, although details of potential interactions between the arch and RNA have been elusive. To understand the interaction of *Saccharomyces cerevisiae* Mtr4 with various RNAs, we have characterized RNA binding in solution using hydrogen-deuterium exchange mass spectrometry, and affinity and unwinding assays. We have identified RNA interactions within the helicase core that are consistent with existing structures and do not vary between tRNA, single-stranded RNA and double-stranded RNA constructs. We have also identified novel RNA interactions with a region of the arch known as the fist or KOW. These interactions are important for RNA unwinding and vary in strength depending on RNA structure and length. They account for Mtr4 discrimination between different RNAs. These interactions further drive Mtr4 to adopt a closed conformation characterized by reduced dynamics of the arch arm and intra-domain contacts between the fist and helicase core.

INTRODUCTION

Eukaryotic RNA processing and surveillance pathways utilize multiple protein complexes to identify and eventually degrade targeted RNA substrates (1–4). Disruption of these pathways can have deleterious effects on a cell and has been associated with a variety of disease states (5–7). Mtr4 plays a central role in nuclear RNA processing and surveillance, providing a bridge between substrate targeting and RNA decay (8,9). Substrate recognition is performed by Mtr4 directly and in association with adaptor complexes such as TRAMP, NEXT or PAXT (3). RNA substrates are delivered through Mtr4 to the exosome, which degrades the RNA with 3′ exonuclease and endonuclease activity. Mtr4 prefers RNA substrates with a 4–6 nucleotide, 3′ single-stranded overhang and accepts a wide range of RNA substrates including rRNA, tRNA, snoRNA, cryptic unstable transcripts, promoter upstream transcripts and others (10–12). The molecular details of how Mtr4 engages with this diverse array of RNAs are poorly understood.

Mtr4 is an essential Ski2-like 3′ to 5′ ATP-dependent RNA helicase (13–15). RNA binding in the Mtr4 helicase core is primarily mediated by recA1, recA2 and the helical bundle (16–18). Protein–RNA interactions involve conserved motifs at the interface of the recA1 and recA2 domains including motifs Ia, Ib, Ic, IV, IVa and V (Supplementary Figure S1a) (19). ATP binding and hydrolysis, on the other hand, involve motifs Q, I, II, III, Va and VI. Motif II includes the catalytic aspartic acid and glutamic acid residues. Other notable features are a β-hairpin in recA2 that is positioned near a double-stranded substrate, as well as a ratchet helix in the helical bundle involved in RNA sequence recognition (20). RNA interactions with the arch are less well defined. The fist in isolation has been shown to interact with structured RNAs, such as double-stranded (ds) RNA and tRNA, but not with single-stranded (ss) RNA (16,21–23). The only structural support for arch engagement with RNA in the context of full-length Mtr4 is a low resolution (8.2 Å) cryo-EM map derived from a sub-population of particles where the fist appears to engage with an RNA-DNA substrate simultaneously engaged in the helicase core (18).

To further investigate *Saccharomyces cerevisiae* Mtr4 binding to various RNA substrates, we have performed hydrogen-deuterium exchange mass spectrometry (HDX),

as well as affinity and unwinding assays. We show that RNA interactions in the helicase core are identical between tRNA, ssRNA, and short and long dsRNA substrates. These interactions are consistent with previous structural studies but do not account for different affinities to Mtr4. However, we also detect interactions between the fist and RNA that do vary depending on RNA structure and length. These interactions reduce the dynamics of the arm and place Mtr4 in a closed conformation defined by the fist being near the surface of recA2. We show that the compromised RNA binding due to removal of the fist also compromises unwinding activity. Taken together, our data reveal an important role for the arch in RNA recognition and demonstrate a connection between arch–RNA interactions and unwinding activity.

MATERIALS AND METHODS

Protein preparation

The *S. cerevisiae* Mtr4$^{\Delta F}$ was constructed by removing residues 667–813 and inserting a three-glycine linker using the Q5 Site-Directed Mutagenesis Kit (NEB). All Mtr4 proteins were recombinantly expressed in *Escherichia coli* BL21-CodonPlus (DE3)-RIPL (Stratagene) using an autoinduction protocol [24]. The purification of Mtr4 was carried out as previously described with the addition of a Hi-Trap DEAE Sepharose FF (GE) before gel filtration [25]. RNase contamination was monitored with an RNaseAlert® kit (IDT) following heparin chromatography and at each subsequent chromatography step. Only RNase-free fractions were retained. Purified Mtr4 with 30% (v/v) glycerol was flash frozen in liquid nitrogen for storage.

RNA preparation

tRNA$_i^{Met}$ is similar to the native tRNA$_i^{Met}$ sequence from *S. cerevisiae* with a CCA cap and poly(A) sequence on the 3′ end. The sequence also includes non-native 5′ and 3′ cloning artifacts. The tRNA$_i^{Met}$ was generated using *in vitro* transcription with T7 RNA polymerase (ThermoFisher Scientific) on a plasmid linearized after the tRNA$_i^{Met}$ sequence. The tRNA$_i^{Met}$ was purified under non-denaturing conditions as previously described [26]. Briefly, the transcription reaction was loaded onto HiTrap DEAE Sepharose FF (GE) and the tRNA$_i^{Met}$ eluted off using a NaCl gradient. All other RNAs were synthesized commercially (Integrated DNA Technologies, Inc.).

Hydrogen-deuterium exchange mass spectrometry

Samples for the initial experiment (Figures 1 and 2) were prepared from stocks of 12.5 μM Mtr4^{WT} with or without 67.5 μM tRNA$_i^{Met}$ (5.4-fold). Samples for subsequent experiments (Figures 3–6) were prepared from stocks of 12.5 μM Mtr4^{WT} or Mtr4$^{\Delta F}$ with or without 25 μM RNA (2-fold). In both cases, stocks were prepared in 50 mM HEPES, 100 mM NaCl, 0.5 mM MgCl$_2$, 0.2 mM TCEP, pH 6.5 and incubated for 10 min at 25°C. Following incubation, samples were diluted 2:23 with the same buffer containing H$_2$O for controls (pH$_{read}$ = 6.5 at 25°C) or D$_2$O for exchange samples (pH$_{read}$ = 6.1 at 25°C; final D$_2$O of 92%). Exchange

proceeded at 25°C for 10, 10^2, 10^3, 10^4 or 10^5 s. Exchange was quenched by mixing samples 1:1 with cooled 1% (v/v) formic acid, 3.84 M guanidinium chloride, pH 1.75 (1:1 mix had a final pH of 2.3 at 0°C) and flash frozen in liquid nitrogen. Samples were prepared in triplicate and stored at −80°C.

Samples were thawed for 50 s immediately prior to injection into a Waters™ HDX manager in line with a SYNAPT G2-Si. In the HDX manager, samples were digested by *Sus scrofa* Pepsin A (Waters™ Enzymate BEH) at 15°C and the peptides trapped on a C4 pre-column (Waters™ Acquity UPLC Protein BEH C4) at 1°C using a flowrate of 100 μl/min for 3 min for the initial experiment or 6 min for subsequent experiments. The chromatography buffer was 0.1% (v/v) formic acid. Peptides were then separated over a C18 column (Waters™ Acquity UPLC BEH) at 1°C and eluted with a linear 3–40% (v/v) acetonitrile gradient using a flowrate of 40 μl/min for 7 min. Samples were injected in a random order.

Mass spectrometry data were acquired using positive ion mode in either HDMS or HDMS^E mode. Peptide identification of water-only control samples was performed using data-independent acquisition in HDMS^E mode. Peptide precursor and fragment data were collected via collision-induced dissociation at low (6 V) and high (ramping 22–44 V) energy. HDMS mode was used to collect low energy ion data for all deuterated samples. All samples were acquired in resolution mode. Capillary voltage was set to 2.8 kV for the sample sprayer. Desolvation gas was set to 650 L/h at 175°C. The source temperature was set to 80°C. Cone and nebulizer gas was flowed at 90 L/h and 6.5 bar, respectively. The sampling cone and source offset were both set to 30 V. Data were acquired at a scan time of 0.4 s with a range of 100–2000 m/z. Mass correction was done using [Glu1]-fibrinopeptide B as a reference. For ion mobility, the wave velocity was 700 ms^{-1} and the wave height was 40 V.

Raw data of Mtr4 water-only controls were processed by PLGS (Waters™ Protein Lynx Global Server 3.0.2) using a database containing *S. scrofa* Pepsin A and *S. cerevisiae* Mtr4^{WT} or Mtr4$^{\Delta F}$. In PLGS, the minimum fragment ion matches per peptide was 3 and methionine oxidation was allowed. The low and elevated energy thresholds were 250 and 50 counts, respectively, and overall intensity threshold was 750 counts. DynamX 3.0 was used to search the deuterated samples for peptides with 0.3 products per amino acid and 1 consecutive product found in 2 out of 7–10 controls. Data were manually refined. Structural images were made using scripts from DynamX in The PyMOL Molecular Graphics System, Version 2.4 (Schrödinger, LLC); and heat maps were made using HD-eXplosion [27]. To allow access to the HDX data of this study, the HDX data summary table (Table 1) and the HDX data table (Supplementary Table S1) are included. Theoretical maximum D-uptake used in percent calculations was determined as follows: 0.92 × (residues in peptide – 1 for N-terminal residue – the number of prolines not at the N-terminal position). Back exchange was calculated using peptides from the Mtr4 only sample that had plateaued (<2% difference in D-uptake at 10^4 and 10^5 s) and had a D-uptake >40%. The number reported in Table 1 is (100 – the average % D-uptake for these peptides at 10^4

Table 1. Summary of HDX experiments

	Mtr4^{WT} Figures 1 and 2	Mtr4^{WT} Figure 3	Mtr4^{WT} Figures 4 and 5	Mtr4$^{\Delta F}$ Figure 6
Ligands	Apo tRNA$_i^{Met}$	apo	apo	apo
	-	tRNA$_i^{Met}$	tRNA$_i^{Met}$	tRNA$_i^{Met}$
	-	ssRNA^{42}	ssRNA^{42}	ssRNA^{42}
	-	-	dsRNA^{32}	dsRNA^{32}
	-	-	dsRNA^{16}	dsRNA^{16}
[Mtr4] (μM)	1	1	1	1
[RNA] (μM)	5.4	2	2	2
HDX buffer	50 mM HEPES, 100 mM NaCl, 0.5 mM MgCl$_2$, 0.2 mM TCEP, pH$_{read}$ = 6.1			
HDX time course	10^1, 10^2, 10^3, 10^4, 10^5 s at 25°C			
HDX control samples	Mtr4^{WT}			Mtr4$^{\Delta F}$
Back exchange (%)	31	38	33	34
Significance cutoffs	ΔHDX > 0.5 Da and P-value < 0.01 in Welch's t-test (n = 3)			
# Peptides	339	188	191	161
Sequence coverage (%)	81	58	58	64
Average peptide length	12.6	9.86	11.08	9.7
Peptide redundancy	5.14	3.21	3.38	2.82
Technical replicates	3	3	3	3
Mean SD	0.064	0.061	0.051	0.050

s). The number of peptides used in the calculation was 90, 75, 32 and 23, from left to right in Table 1. The raw mass spectrometry data are available from ProteomeXchange via the PRIDE partner repository with identifier PXD031962.

Affinity measurements

Dissociation constants (K_d) between Mtr4 and RNA were measured using an electrophoretic mobility shift assay. Various concentrations of Mtr4^{WT} or Mtr4$^{\Delta F}$ were mixed with 60 nM RNA in binding buffer (40 mM MOPS, 100 mM NaCl, 0.5 mM MgCl$_2$, 5% [v/v] glycerol, 0.01% [v/v] nonidet-P40 substitute, 1 U/μl of Ribolock [ThermoFisher Scientific], 2 mM dithiothreitol, pH 6.5). Samples were incubated on ice for 45–60 min to reach equilibrium and diluted 1:4 with loading buffer (20% [v/v] glycerol, 0.1% [w/v] bromophenol blue, 0.1% [v/v] xylene cyanol). Aliquots were separated on a native 4–20% gradient polyacrylamide TBE gel for 80–210 min at 120 V. The gel was stained with SYBR Gold Nucleic Acid Gel stain (Invitrogen) and imaged with a ChemiDoc MP Imaging system (Bio-Rad Laboratories). The fraction of RNA bound was quantified by densitometry using Image Lab (Bio-Rad Laboratories) and fit to a quadratic ($\theta = ([A] + [B] + Kd) - \sqrt{(([A] + [B] + Kd)^2 - 4 \times [A] \times [B])/2})$), where θ is fraction bound, $[A]$ is total concentration of Mtr4, $[B]$ is the total concentration of RNA, and Kd is the dissociation constant. Data were fit using KaleidaGraph (Synergy Software).

RNA unwinding assays

Pre-steady state unwinding assays were performed essentially as described (12,20,28). Unwinding activity was determined by monitoring the displacement of a 16-nt RNA labeled with a fluorescein on its 5′ end, from a longer unlabeled RNA strand when incubated with Mtr4 at saturating levels of ATP. Unwinding reactions were performed in 40 mM MOPS, 100 mM NaCl, 0.5 mM MgCl$_2$, 5% (v/v) glycerol, 0.01% (v/v) nonidet-P40 substitute, 1 U/μl of Ribolock (ThermoFisher Scientific), 2 mM dithiothreitol, pH 6.5 at 30°C. About 50–1200 nM of Mtr4 was incubated with 10 nM fluorescein-labeled duplex RNA and 100 nM DNA-trap oligonucleotide for 5 min. Reactions were initiated by the addition of 1.6 mM ATP with MgCl$_2$. At various times aliquots were quenched with a 1:1 dilution in 1% (v/v) SDS, 5 mM EDTA, 20% (v/v) glycerol. Samples were separated on a 15% native polyacrylamide TTE gel for 80 min at 120 V. Gels were imaged with a ChemiDoc MP Imaging system (Bio-Rad Laboratories).

RESULTS

To characterize the solution interaction between *S. cerevisiae* Mtr4 and RNA we employed bottom-up HDX. HDX measures deuterium incorporation into the amide groups of the protein backbone with the rate of incorporation being a readout for H-bonding and solvent accessibility. We recovered over 300 peptides redundantly spanning 81% of the Mtr4 sequence (Table 1 and Supplementary Table S1). The longest stretch lacking peptides was the disordered N-terminal tail (Supplementary Figure S1c). We monitored the deuterium uptake of all peptides in Mtr4 alone and bound by RNA. For Mtr4 alone, the absolute amount of deuterium uptake correlated well with known secondary and tertiary structural elements. Deuterium uptake was lowest in the globular recA domains and highest in the N-terminal sheet and parts of the arch. The N-terminal sheet and arch are likely mobile and solvent exposed when Mtr4 is alone in solution. This is in keeping with the various orientations of the arch observed in structures of Mtr4 from yeast, human and plants (16,29,30).

tRNA$_i^{Met}$ binds Mtr4 at the interface of the recA1 and recA2 domains

To identify changes in Mtr4 upon binding RNA, we first compared deuterium uptake of Mtr4 alone to that of Mtr4 with a hypomodified tRNA$_i^{Met}$. Hypomodified tRNA$_i^{Met}$

Table 2. Dissociation constants of Mtr4^{WT} or Mtr4$^{\Delta F}$ to various RNAs. The dissociation constants (K_d) between Mtr4^{WT} or Mtr4$^{\Delta F}$ and tRNA$_i$^{Met}, ssRNA^{42}, dsRNA^{32} or dsRNA^{16} were measured using an electrophoretic mobility shift assay (Supplementary Figure S6). K_d values are an average of three independent gels plus or minus one SD. The ratio between Mtr4$^{\Delta F}$ and Mtr4^{WT} is listed to one significant figure

	$K_d \pm$ SD (μM)		
	Mtr4^{WT}	Mtr4$^{\Delta F}$	*Ratio*
tRNA$_i$^{Met}	0.27 ± 0.02	1.94 ± 0.16	*7*
ssRNA^{42}	0.42 ± 0.04	1.16 ± 0.13	*3*
dsRNA^{32}	0.57 ± 0.03	2.99 ± 0.23	*5*
dsRNA^{16}	1.14 ± 0.08	1.42 ± 0.22	*1*

is a native substrate of Mtr4 and our construct had a 12-nucleotide, 3′ overhang with sequence A$_9$CGC (Supplementary Table S2) [15]. We determined the dissociation constant (K_d) between full-length Mtr4 (Mtr4^{WT}) and tRNA$_i$^{Met} to be 0.27 ± 0.02 μM (± SD; Table 2). Based on this we used a 5.4-fold excess of tRNA$_i$^{Met} to ensure at least 90% of Mtr4^{WT} was RNA-bound. Throughout this work, we show the difference in deuterium uptake between Mtr4 alone and RNA-bound using heatmaps created with HD-eXplosion [27]. The red shading indicates a statistically significant difference or protection upon RNA binding. We defined significance as a decrease ≥ 0.5 Da and a P-value ≤ 0.01 in a Welch's t-test (n = 3). Such significant decreases in deuterium uptake upon addition of tRNA$_i$^{Met} were observed in all domains of Mtr4^{WT}, except the N-terminal sheet and the winged-helix (Figure 1A, D).

The decreases in deuterium uptake seen in the helicase core upon addition of tRNA$_i$^{Met} are consistent with previous RNA-bound Mtr4 structures. The 'core' refers to the domains shared with most other helicases and includes the recA1, recA2, winged-helix and helical bundle domains (Supplementary Figure S1a). In the recA1, the largest protection occurred in two regions near the RNA (Figures 1B and 2). The first region contains motif 1a directly involved in RNA binding, while the second region is near motif II and the catalytic residues. Protection was also seen for RNA-binding motifs 1b and 1c, albeit less than motif 1a. In the recA2, protection similarly occurred in motif IV situated near the RNA backbone, and a β-hairpin wedge that purportedly acts to split RNA strands (Figures 1C and 2) [18,31]. Protection was also seen for motifs IVa, V and VI, but less than motif IV and the β-hairpin wedge. Small decreases also occurred in the helical bundle, specifically in a region that sits atop the RNA bases, and in the single peptide (1016–1023) near the ratchet helix that recognizes the 3′ overhang (Figures 1F and 2) [20].

The broad agreement between high-resolution structures and the regions protected from deuterium exchange reinforces that the tRNA$_i$^{Met} 3′ overhang binds at the interface of the recA1 and recA2 (Figure 2). The data show that this occurs in solution and in the context of a large and folded tRNA substrate for which a co-structure with Mtr4 is not available. Motifs 1a, II, IV and the β-hairpin wedge emerge as being the most important for RNA binding, as within the helicase core they show the largest protection at any one

time point (Figure 1B–D, F). These regions are also characterized by a particular kinetic profile with protection being sustained throughout almost the entire HDX time course. The sustained decrease is highlighted by uptake plots of example peptides (Supplementary Figure S1b). Such a kinetic profile is thus likely characteristic of an RNA-binding region in Mtr4.

### Binding of tRNA$_i$^{Met} stabilizes a closed conformation of Mtr4

Addition of tRNA$_i$^{Met} to Mtr4^{WT} also caused a decrease in deuterium uptake in the arch. The arch contains an arm composed of two sets of anti-parallel helices (designated here as helices 1 and 4; and helices 2 and 3) with a fist domain inserted between helices 2 and 3 (Supplementary Figure S1a). Structural work has shown that the arch can adopt various positions relative to the core. In some Mtr4 structures the fist of the arch is positioned near to recA2, while in others the fist is solvent exposed to varying degrees [8]. We define the conformation where the fist is in contact with the recA2 as a closed conformation of Mtr4. Upon addition of tRNA$_i$^{Met}, we observed a decrease in uptake in both the fist and the arm of the arch (Figure 1E).

Within the fist, the largest protection occurred in a loop that in closed Mtr4 forms a continuous surface with the established RNA-binding site and β-hairpin wedge (Figure 2). This protection is likely attributed to direct RNA-binding due to the loop's location, as well as the kinetic profile of protection. Protection of the loop persisted throughout the entire HDX time course, similar to the known RNA-binding regions (Figure 1E and Supplementary Figure S1b). Direct binding of the fist to dsRNA has previously been reported using an isolated fist construct [23]. Reduced deuterium uptake also extended to the opposite side of the fist, distal to the RNA (Figure 2). In closed Mtr4, this opposite side interacts with a surface of recA2, and we observed a similar decrease in uptake at this recA2 surface. This suggests that the fist contacts the recA2 in the presence of tRNA$_i$^{Met} (Figure 1C, E). It seems likely that the fist directly binds the tRNA$_i$^{Met} through a loop and is then positioned near recA2, putting Mtr4 in a closed conformation.

The data further show that tRNA$_i$^{Met} causes a drastic change in the conformational plasticity of the four helices of the arm. Of all the Mtr4^{WT} regions, the arm had the largest reduction in deuterium uptake upon addition of tRNA$_i$^{Met} (Figures 1E and 2). The kinetic profile of the decreased uptake was also distinct from that associated with RNA binding by the helicase core and fist. Rather than showing a sustained decrease throughout the entire HDX time course, the arm showed a relatively short-lived decrease that appeared at 10^2 s and was diminished by 10^4 s (Figure 1E and Supplementary Figure S1b). The distinct exchange profile, combined with the fact that previous structures show no direct association between the arm and RNA, suggests the protection to be a result of a conformational change. Binding to the tRNA$_i$^{Met} seems to constrain the arch to one or a subset of conformations due to contacts formed between the fist and both tRNA$_i$^{Met} and recA2, placing Mtr4 into a closed conformation.
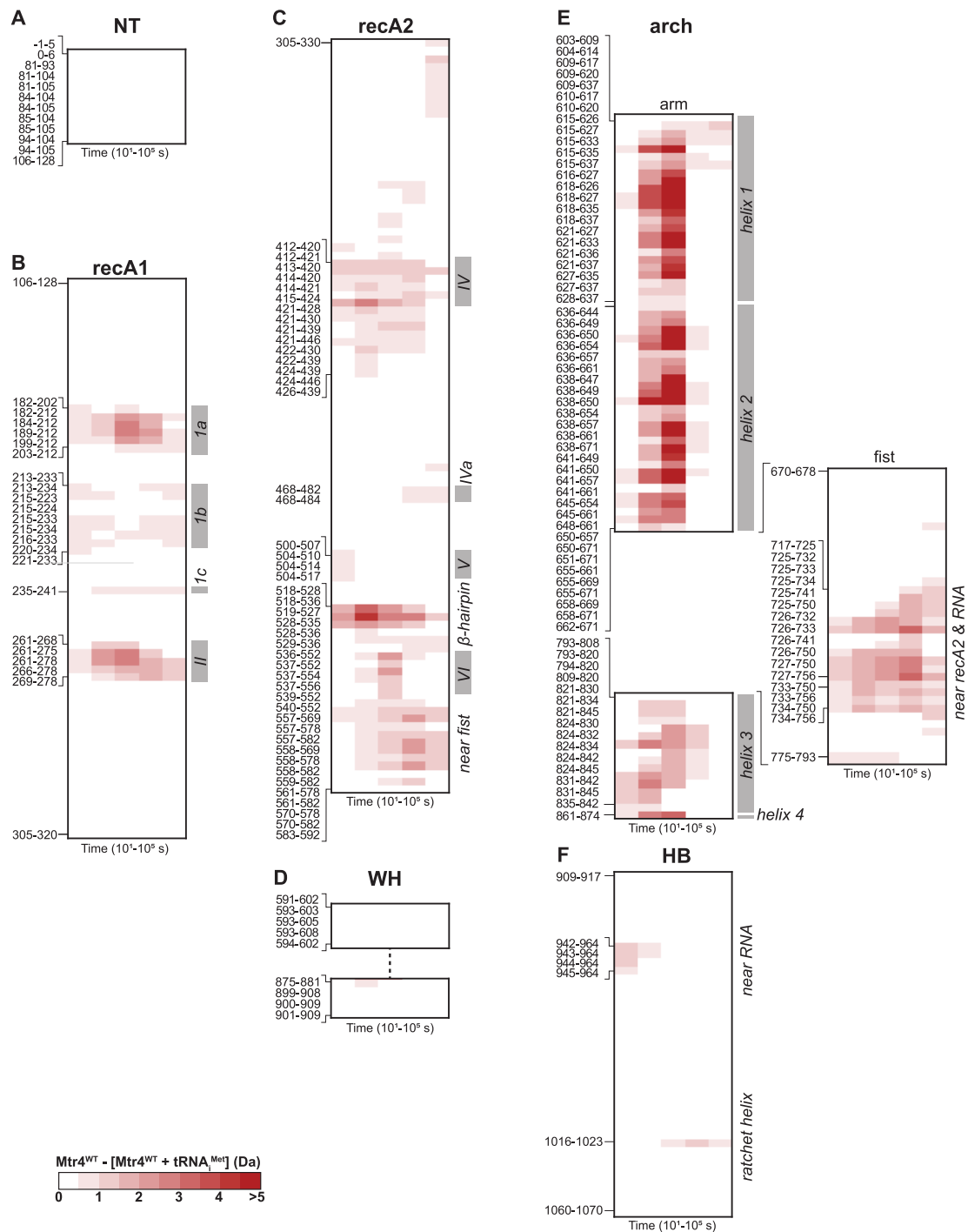
Figure 1. Addition of tRNA$_i$^Met caused reduced deuterium uptake in several domains of Mtr4^{WT}. Heatmaps showing the difference in deuterium uptake between Mtr4^{WT} alone and Mtr4^{WT} with 5.4-fold tRNA$_i$^Met. Peptides were recovered from the following domains: (**A**) N-terminal (NT), (**B**) recA1, (**C**) recA2, (**D**) winged-helix (WH), (**E**) arch and (**F**) helical bundle (HB). The time points of exchange (*x*-axis) were 10, 10^2, 10^3, 10^4 and 10^5 s. Red blocks indicate a difference ≥0.5 Da with a *P*-value ≤ 0.01 in a Welch's *t*-test (*n* = 3). Boundaries of peptides with significant changes are shown (left, *y*-axis) and Mtr4 features are labeled (right, *y*-axis). Example uptake plots and a full list of peptides are in Supplementary Figure S1b,c. Figure was created using HD-eXplosion (27). In this study, Mtr4 numbering does not include the start methionine (Supplementary Table S1).
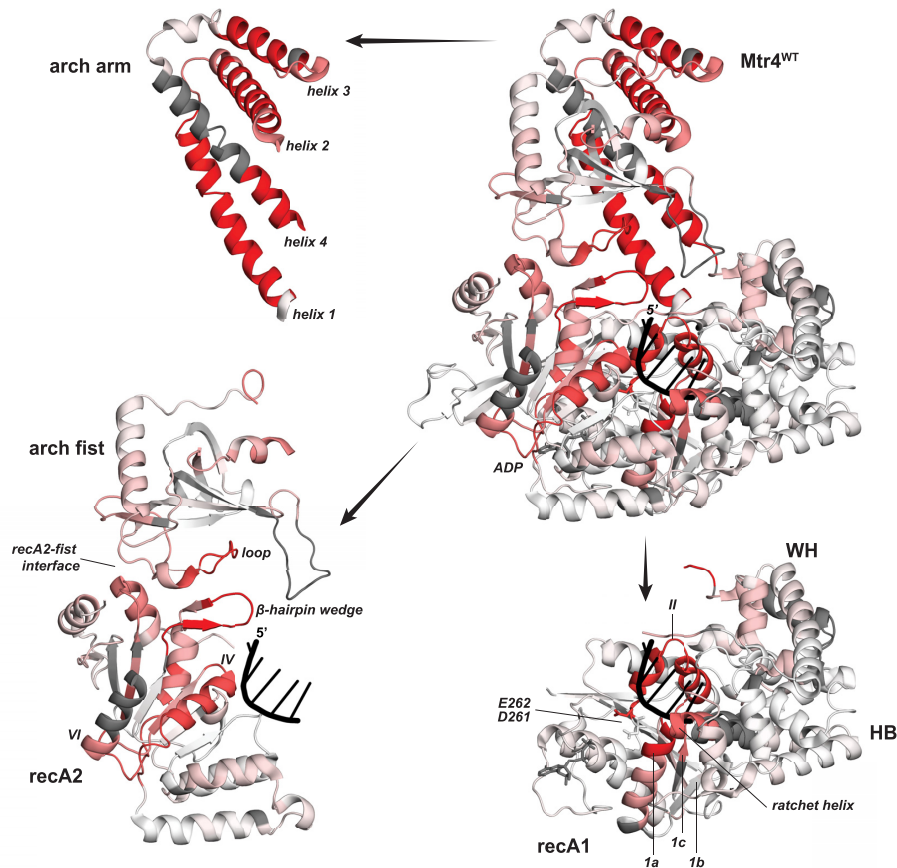
Figure 2. The helicase core and arch of Mtr4[WT] showed reduced deuterium uptake in the presence of tRNA$_i$[Met]. Mtr4 (PDB 2XGJ Chain A) is colored by the difference in fractional deuterium uptake between Mtr4[WT] alone and Mtr4[WT] with 5.4-fold tRNA$_i$[Met] after 10^3 s exchange. The scale is 0–20% (white to red) and is based on DynamX residue-level scripts without statistical filtering from the data shown in Figure 1. Residues without coverage are grey and Mtr4[WT] features are labeled including ADP (gray sticks), RNA (black) and D261-E262 (sticks). The images depict the entire Mtr4[WT] structure (top right), the arm of the arch (top left), the fist and recA2 (bottom left), and the recA1, WH and HB (bottom right).

RNA interactions outside the helicase core account for Mtr4 substrate preference

We next characterized Mtr4 binding to ssRNA. We used a 42-nucleotide ssRNA with a polyadenylated tail at its 3′ end (ssRNA[42]) (Supplementary Table S2). The 3′ poly(A) included five adenines as this is the ideal length to maximize binding to Mtr4 (32). ssRNA[42] is not predicted to have any secondary structure or to dimerize (based on IDT Oligo-Analyzer tool) and was designed to be long enough to traverse the helicase core and the fist. We determined the affinity of ssRNA[42] to Mtr4[WT] to be 0.42 ± 0.04 μM ($\pm$ SD; Table 2); 1.6-fold weaker than the binding of tRNA$_i$[Met] (Table 2). This reduced binding, combined with large amounts of ssRNA[42] being problematic in our HDX system, limited our ability to saturate Mtr4[WT] during the exchange reaction. Instead, we used a 2-fold excess of ssRNA[42] over Mtr4[WT] and repeated the experiment with tRNA$_i$[Met] under this same excess (all peptides shown in Supplementary Figure S2). The dataset had less usable peptides than the previous dataset due to RNA-induced peptide carryover but still contained almost 200 peptides covering 58% of the Mtr4[WT] sequence (Table 1 and Supplementary Table S1). This facilitated direct comparison of Mtr4[WT] binding to ssRNA[42]

and tRNA$_i$[Met]. The Mtr4[WT] regions altered by tRNA$_i$[Met] were broadly similar when it was 2-fold and 5.4-fold (compare Figure 1 and Supplementary Figure S2; Figure 6C).

Comparison of ssRNA[42] and tRNA$_i$[Met] revealed identical decreases in deuterium uptake in the core RNA-binding elements of Mtr4[WT] (Figure 3, black). Important motifs 1a, IV, the β-hairpin wedge and the ratchet helix, all showed the same degree of protection upon addition of either ssRNA[42] or tRNA$_i$[Met]. While the involvement of the same regions is not surprising, the identical magnitude of protection was unexpected given the difference in their binding affinities for Mtr4[WT] (Table 2). This demonstrates that the difference must be due to binding interactions outside of the Mtr4[WT] helicase core. Outside of the helicase core, addition of ssRNA[42] caused less protection than tRNA$_i$[Met] (Figure 3, gray). Less protection was seen in the fist and arm of the arch, as well as at the surface of recA2. The smaller effect of ssRNA[42] compared to tRNA$_i$[Met] outside the helicase core tracks with their relative affinities for Mtr4[WT]. Thus, regions outside of the Mtr4 helicase core are responsible for the enhanced affinity of tRNA$_i$[Met] compared to ssRNA[42]. These regions function in addition to those in the helicase core that are equally used by both RNA types.
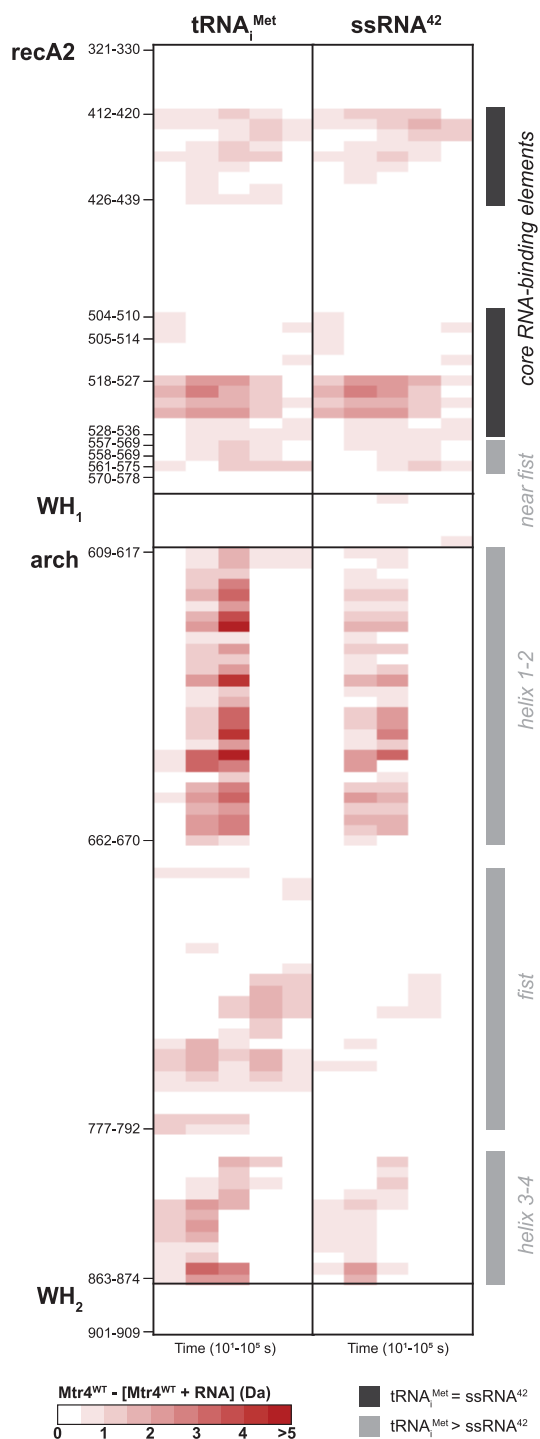
Figure 3. Protection in the arch of Mtr4[WT] was reduced for ssRNA[42] compared to tRNA$_i$[Met]. Heatmaps showing the difference in deuterium uptake between Mtr4[WT] alone and Mtr4[WT] with 2-fold tRNA$_i$[Met] or ssRNA[42]. Peptides from the recA2, WH (split into WH$_1$ and WH$_2$), and arch are shown with domain boundaries and key peptides (left, *y*-axis) indicated. The complete data set is shown in Supplementary Figure S2. The time points of exchange (*x*-axis) were 10, 10[2], 10[3], 10[4] and 10[5] s. Red blocks indicate a difference ≥0.5 Da with a *P*-value ≤ 0.01 in a Welch's *t*-test (*n* = 3). Mtr4 features are labeled (right, *y*-axis) with black indicating equal difference between tRNA$_i$[Met] and ssRNA[42] and gray indicating less difference for ssRNA[42] than tRNA$_i$[Met]. Figure was created using HD-eXplosion (27).

Table 3. Unwinding rate of Mtr4[WT] or Mtr4[ΔF] with dsRNA[16] or dsRNA[32] substrates. The maximum strand-separation rate constants (k_{uwn}[max]) for Mtr4[WT] or Mtr4[ΔF] were measured using dsRNA[32] or dsRNA[16] as substrate. k_{uwn}[max] values are an average of three independent experiments plus or minus one SD. The ratio between Mtr4[ΔF] and Mtr4[WT] is listed to one significant figure. The data for Mtr4[WT] with dsRNA[16] are from previously published work (20)

|	k_{uwn}[max] $\pm$ SD (min^{-1})		
	Mtr4[WT]	Mtr4[ΔF]	*Ratio*
dsRNA[32]	0.56 ± 0.04	0.25 ± 0.02	*0.4*
dsRNA[16]	0.59 ± 0.05[a]	0.56 ± 0.07	*0.9*

[a]Previously published (20).

The data with ssRNA[42] provides several additional insights into RNA binding by Mtr4[WT]. The first is that the fist does in fact form contacts with ssRNA[42] as the ssRNA[42] did induce protection, albeit less than tRNA$_i$[Met] (Figure 3). This differs from previous work showing that the isolated fist can bind dsRNA but not ssRNA (21,22). Contacts between the fist and ssRNA are likely promoted in full-length Mtr4 as the RNA would be tethered nearby by tight interactions in the helicase core. Another insight is the apparent connection between the arm and fist of the arch, and the surface of recA2. These regions showed a very similar reduction in protection when tRNA$_i$[Met] was replaced with ssRNA[42] (Figure 3). This suggests that RNA-binding by the fist, conformational change in the arm, and interactions between the fist and recA2 surface, are coupled events that result in RNA-bound Mtr4 adopting a so-called closed conformation. Further, this closed conformation appears grossly similar for Mtr4 bound by either tRNA$_i$[Met] or ssRNA[42]. The latter is indicated by the similar pattern of protection upon addition of either type of RNA (Figure 3).

The Mtr4 arch senses the type of RNA

To further characterize the RNA features recognized by Mtr4, we made use of two dsRNA constructs. These constructs have been used to characterize the nucleic acid unwinding rate by Mtr4 (Table 3) (32). One construct had a 16-bp duplex with a 6-nucleotide, 3′ overhang of UAAAAA, which is approximately the same length as the acceptor stem, T-arm and T-loop of the tRNA$_i$[Met] (dsRNA[16]; Supplementary Table S2). The other construct was similar but had an extended duplex (32 bp) with a hairpin and a nick (dsRNA[32]; Supplementary Table S2). The dsRNA[32] is approximately the same number of base pairs as tRNA$_i$[Met], although it likely adopts a different fold. Both dsRNA[32] and dsRNA[16] had reduced binding to Mtr4[WT] compared to tRNA$_i$[Met]. The affinities were 0.57 ± 0.03 and 1.14 ± 0.08 μM (± SD; Table 2); 2- and 4-fold weaker than tRNA$_i$[Met], respectively. The different binding affinities of dsRNA[16], dsRNA[32] and tRNA$_i$[Met] show that Mtr4 affinity is influenced by the fold and/or the length of the RNA.

Given the different affinities of the dsRNA constructs, we performed another HDX experiment to directly compare their binding to Mtr4[WT]. We again used a 2-fold excess of dsRNA over Mtr4[WT] and included both tRNA$_i$[Met] and ssRNA[42] for direct comparison (Table 1, Supplemen-
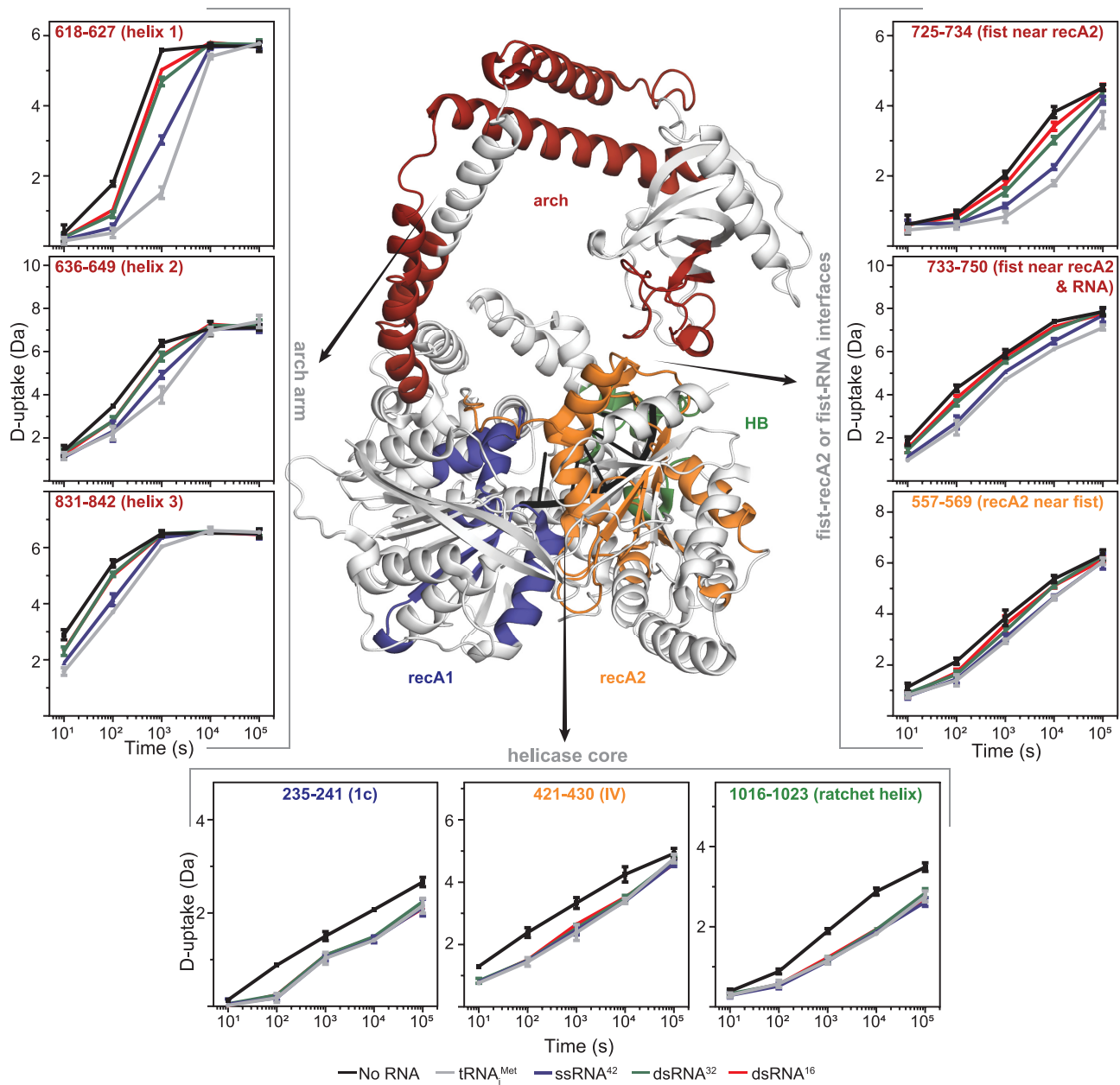
Figure 4. Deuterium uptake in the arch, but not the helicase core, of Mtr4[WT] was influenced by RNA type. Mtr4 (PDB 2XGJ Chain A) surrounded by example uptake plots from the arch arm (left), fist and recA2 surface (right), and helicase core (bottom). Uptake plots show Mtr4[WT] alone (black) and with 2-fold tRNA$_i$[Met] (gray), ssRNA[42] (blue), dsRNA[32] (green) or dsRNA[16] (red). Plotted uptake is the average of three replicates and error bars are plus or minus two SD. The *y*-axis range is 80% of theoretical maximum uptake, assuming the N-terminal residue undergoes complete back-exchange. Data have not been corrected for back-exchange. Heatmap for all peptides from this dataset is in Supplementary Figure S3. Colors on the Mtr4 structure show regions protected by 5.4-fold tRNA$_i$[Met] (based on data in Figure 1) in the recA1 (blue), recA2 (orange), arch (red) and HB (green) domains.

tary Table S1; all peptides shown in Supplementary Figure S3a,b). The Mtr4[WT] regions altered by tRNA$_i$[Met] and ssRNA[42] were similar between replicate experiments (compare Supplementary Figure S2 and S3a,b; Figure 6C). Concurrent analysis of all four RNA constructs showed identical decreases in deuterium uptake in the core RNA-binding elements of Mtr4[WT] (Supplementary Figure S3a,b). RNA-binding motifs 1a, 1c, IV and the ratchet helix, all had the same degree of protection regardless of the type of RNA added (example peptides shown in Figure 4). This shows

that dsRNA[16], dsRNA[32], ssRNA[42] and tRNA$_i$[Met] all bind to the helicase core in the same manner and with the same affinity. RNA features seem to have little to no effect on Mtr4 binding to the 3′ RNA tail. This reinforces the conclusion that differences in RNA affinity for Mtr4[WT] are dictated by interactions outside of the helicase core.

In contrast to the helicase core, the degree of protection in the arch was less for both dsRNAs compared to either the ssRNA[42] or tRNA$_i$[Met]. This reduced protection was seen in all helices of the arm, the fist, and at the surface
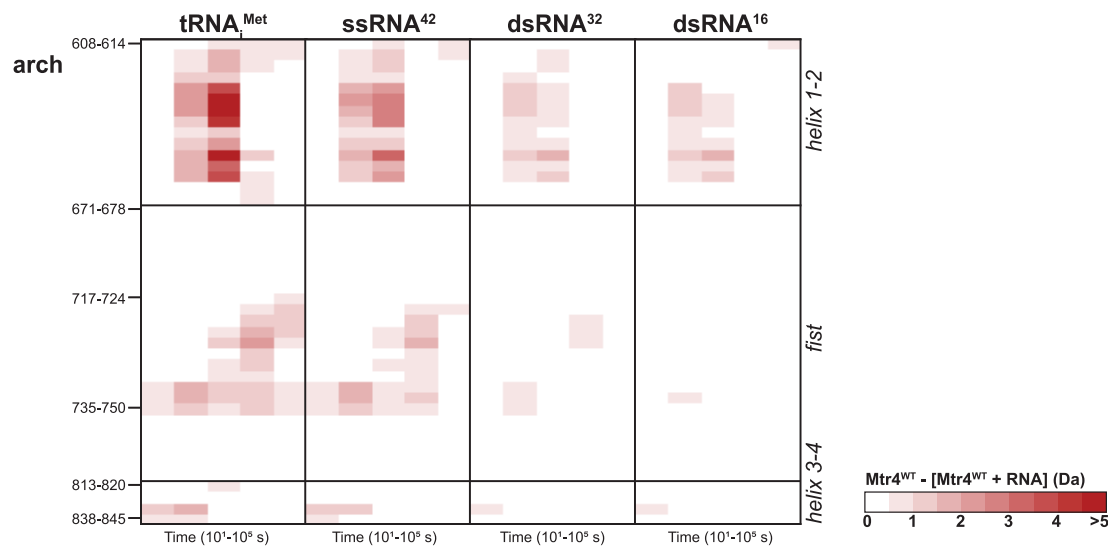
Figure 5. The degree of protection in the arch of Mtr4^{WT} varied with RNA type. Heatmaps showing the difference in deuterium uptake between Mtr4^{WT} alone and Mtr4^{WT} with 2-fold tRNA$_i^{Met}$, ssRNA^{42}, dsRNA^{32} or dsRNA^{16}, for peptides from the arch. The complete data set is shown in Supplementary Figure S3. The time points of exchange (*x*-axis) were 10, 10^2, 10^3, 10^4 and 10^5 s. Key peptides (left, *y*-axis) and Mtr4 features (right, *y*-axis) are labeled. Red blocks indicate a difference ≥0.5 Da with a *P*-value ≤ 0.01 in a Welch's *t*-test (*n* = 3). Figure was created using HD-eXplosion (27).

of recA2 (Figures 4, 5 and Supplementary Figure S3a,b). The reduced protection is in line with the weaker binding affinities of the dsRNAs (Table 2) and suggests that the fist has less, or more transient, interactions with the dsRNAs compared to ssRNA^{42} or tRNA$_i^{Met}$. The reduced protection in the arm, fist and recA2 surface reinforces the connection between RNA-binding and arch movement. Close inspection of the data further shows greater protection for dsRNA^{32} than dsRNA^{16} (Figure 5). This is clearer when a cutoff of 0.3 Da (rather than 0.5 Da) is used (Supplementary Figure S3c). A cutoff of 0.3 Da is justified as the standard error of the mean with a Student's *t*-distribution value for 0.05 significance, gives approximately 0.22 Da for each of the data sets (33). Altogether, comparison of the four RNA substrates shows unequivocally that the contribution of the arch depends on the type of RNA.

Fist interactions with RNA drive Mtr4 conformational change

In parallel to varying the RNA substrate, we characterized a fist-less Mtr4 (Mtr4$^{\Delta F}$) with residues 667–813 replaced by a three-glycine linker. Removal of the fist reduced binding of tRNA$_i^{Met}$, ssRNA^{42} and dsRNA^{32} by 7-, 3- and 5-fold, respectively (Table 2). This reduction suggests that the fist directly contributes to recognition of these RNAs and is consistent with the similar kinetics of protection seen for the helicase core and the fist in the HDX with Mtr4^{WT} (Figures 1 and 3). The larger effect of fist removal on binding dsRNA^{32} compared to ssRNA^{42} was surprising and may be due to binding differences not apparent when using Mtr4^{WT}. Unlike tRNA$_i^{Met}$, ssRNA^{42} and dsRNA^{32}, the removal of the fist did not significantly affect Mtr4 binding to dsRNA^{16}. This shows that the fist plays little to no role in recognition of dsRNA^{16} and is keeping with the low levels of protection seen for the fist in the HDX with Mtr4^{WT} (Figure

5). The 1.5–2.0 μM affinities for Mtr4$^{\Delta F}$ likely represent RNA binding in the helicase core, with the higher affinities of Mtr4^{WT} being attributable to RNA interactions with the fist (Table 2). The affinity differences between Mtr4$^{\Delta F}$ and Mtr4^{WT} thus demonstrate how the fist is directly responsible for fine tuning binding preference depending on RNA features.

We also characterized Mtr4$^{\Delta F}$ binding to the four different RNAs using HDX in the same conditions as used for Mtr4^{WT}. In fact, Mtr4$^{\Delta F}$ and Mtr4^{WT} were exchanged and quenched simultaneously, with the Mtr4$^{\Delta F}$ samples being thawed and injected into the mass spectrometer immediately following the Mtr4^{WT} samples (Tables 1, 2; all peptides shown in Supplementary Figure S4a,b). When compared to Mtr4^{WT} in the absence of RNA, Mtr4$^{\Delta F}$ had similar deuterium uptake in the helicase core and increased uptake in the arch. Compare, for example, peptides 235–241 from the core and peptides 636–649 from the arch, between Mtr4^{WT} (Figure 4, black trace) and Mtr4$^{\Delta F}$ (Figure 6B, black traces). This shows that deletion of the fist did not compromise the structure of the helicase core but did increase the dynamics of the arch when Mtr4 was alone in solution.

The changes in deuterium uptake of Mtr4$^{\Delta F}$ upon addition of RNA were identical for all four of our RNA constructs, but differences were observed between Mtr4$^{\Delta F}$ and Mtr4^{WT}. Reduced uptake was seen in the helicase core of Mtr4$^{\Delta F}$, with equal protection seen upon addition of tRNA$_i^{Met}$, ssRNA^{42}, dsRNA^{32} or dsRNA^{16} (Figure 6B and Supplementary Figure S4a,b). While coverage of some RNA-binding motifs was lacking, protection was seen for motifs 1a, 1c, IV and the ratchet helix (Figure 6C). For these motifs, particularly 1a, the degree of protection was slightly less for Mtr4$^{\Delta F}$ than Mtr4^{WT} (Figure 6A, compare left and right). The interactions between the fist and RNA may thus subtly alter the stability and trajectory of RNA
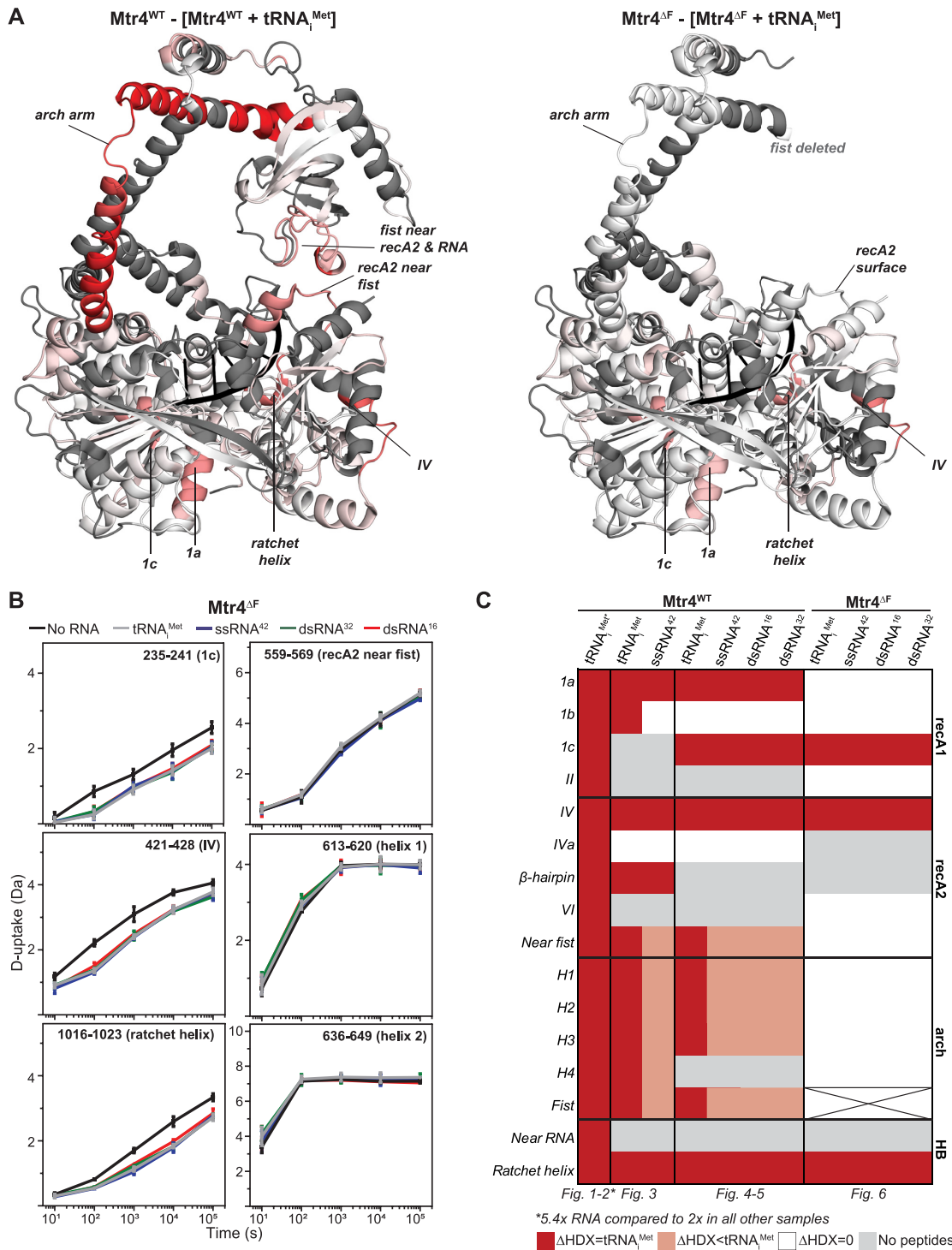
Figure 6. Deletion of the fist in Mtr4$^{\Delta F}$ caused a loss of protection in the arch. (**A**) Mtr4 (PDB 2XGJ Chain A) is colored by the difference in fractional deuterium uptake between Mtr4^{WT} (left) or Mtr4$^{\Delta F}$ (right) alone and with 2-fold tRNA$_i^{Met}$ after 10^3 s exchange. The scale is 0–20% (white to red) and is based on DynamX residue-level scripts without statistical filtering. Residues without coverage are gray. Complete data for Mtr4$^{\Delta F}$ with each RNA is in Supplementary Figure S4. (**B**) Example uptake plots with Mtr4$^{\Delta F}$ alone (black) and with 2-fold tRNA$_i^{Met}$ (gray), ssRNA^{42} (blue), dsRNA^{32} (green) or dsRNA^{16} (red). Plotted uptake is the average of three replicates and error bars are plus or minus two SD. The *y*-axis range is 80% of theoretical maximum uptake, assuming the N-terminal residue undergoes complete back-exchange. Data have not been corrected for back-exchange. (**C**) Summary of all HDX experiments. Mtr4 features (left, *y*-axis) are annotated as having equal (red) or less (light red) protection as the tRNA$_i^{Met}$ sample in the same HDX experiment, no protection (white) or no coverage (gray). The fist of Mtr4$^{\Delta F}$ is crossed.

through the helicase core. A more obvious difference was in the arm, as the large RNA-induced protection seen in Mtr4^{WT} was completely lost in Mtr4$^{\Delta F}$. All helices of the arm and the surface of the recA2 of Mtr4$^{\Delta F}$ had no change in uptake upon addition of RNA (Figure 6). This tracks with the weaker affinity of Mtr4$^{\Delta F}$ for tRNA$_i^{Met}$, ssRNA^{42} and dsRNA^{32}, when compared to Mtr4^{WT}. Removal of the fist clearly prevents the conformational change of the arch revealing that RNA interactions with the fist and not the helicase core drive arch movements. Comparison of Mtr4^{WT} and Mtr4$^{\Delta F}$ identifies a clear role for the fist in binding RNA and regulating Mtr4 transition between unbound and bound states.

To fully ascertain the role of the fist, we used pre-steady state assays to measure the unwinding rate of Mtr4^{WT} and Mtr4$^{\Delta F}$. We compared dsRNA^{32} and dsRNA^{16} substrates as the fist plays a small and large role in their binding respectively (Table 2). Mtr4^{WT} and Mtr4$^{\Delta F}$ unwound the dsRNA^{16} at similar speeds with maximum strand-separation constants at enzyme saturation being ~0.6 min^{-1} (Table 3). This is consistent with the fist playing only a minor role for the short dsRNA^{16}. A similar result was obtained with a completely arch-less Mtr4 (25). Mtr4^{WT} and Mtr4$^{\Delta F}$, however, differed in their ability to unwind dsRNA^{32}, with the deletion mutant being 2-fold slower (Table 3 and Supplementary Figure S5). This shows that the fist contributes to the catalytic unwinding activity that occurs in the helicase core of Mtr4. The interactions between the fist and RNA that drive conformational change of the arch are thus relevant to both the binding and unwinding of RNA by Mtr4.

DISCUSSION

Mtr4 plays an important gatekeeping role for RNA decay in the nucleus, engaging a wide range of RNAs and delivering unwound substrates to the exosome for degradation (10,18). Prior to this work, the molecular underpinnings of Mtr4 preference among the many diverse RNA substrates were not clear. Our solution studies, however, demonstrate that substrate selection is driven by the arch. As most of our experiments were conducted in the absence of ATP, our observations are relevant to RNA binding and recognition events.

In our HDX experiments, we detect RNA interactions with the helicase core that are consistent with known Mtr4-RNA structures (Figures 1 and 2). The observed binding in the core is identical between all RNA substrates. This is notable as our various RNAs do not have identical 3′ overhangs. The tRNA has an overhang of A$_9$CGC, while the other RNAs have A$_5$ (Supplementary Table S2). Any differences in how these overhangs bind the core, if any, must be subtle enough to evade detection in our assay. It is also notable that the RNA features beyond the 3′ overhang do not influence binding in the core in an appreciable way. tRNA, for example, binds the core in an identical fashion to a 42-nt ssRNA. Most significantly, however, similar binding in the core demonstrates that determinants of substrate selectivity, as reflected in varied binding affinities (Table 2), must occur elsewhere, namely in the arch.

Our HDX experiments also reveal RNA-induced protection from exchange in both the arm and fist of the arch. The magnitude of the protection varies depending on RNA type; with tRNA having the largest protection, followed by ssRNA, long dsRNA, and lastly, short dsRNA (Figures 4 and 5). Little to no changes occur in the arch upon the addition of short dsRNA. This shows that arch involvement is a function of both RNA structure and length. Based on kinetic profiles of exchange, we ascribe the changes in the fist to direct interactions with the RNA. This is consistent with previous work showing that a fist-only construct can interact with RNA (16,21). Moreover, the data imply that fist-RNA interactions are enhanced in the context of full-length Mtr4. We observe significant fist interactions with ssRNA (Figure 3), whereas no ssRNA interactions were previously observed for the fist-only construct. Presumably, these interactions are enhanced by the tethering of the RNA to the nearby helicase core.

We further show that fist–RNA interactions are relevant to helicase activity. Removal of the fist reduces the ability of Mtr4 to unwind a 32-bp dsRNA that interacts with the fist but has no effect on unwinding a 16-bp dsRNA that does not interact with the fist (Table 3). This provides an explanation for an earlier observation that removal of the arch has minimal impact on unwinding the 16-bp substrate (25), and further clarifies the molecular basis of previous conclusions that the arch plays a role in unwinding events (20). Direct RNA interactions with the fist appear to facilitate unwinding across larger or more complex substrates. Since Mtr4 will most likely encounter substrates larger than a 16-bp dsRNA *in vivo*, we expect that the arch will be involved in unwinding activity, with the precise details of involvement depending on RNA type. Our model is consistent with a single-molecule study showing that Mtr4 translocates along an RNA strand only when duplex RNA is located immediately upstream (34). We suggest that fist–RNA interactions contribute to this upstream sensing mechanism.

Coupled with the fist–RNA interactions, we detect a conformational change in the arm of the arch. Indeed, fist–RNA interactions drive this conformational change (Figure 6). Although the precise nature of the rearrangement of the arm is unclear, the result is that the fist and recA2 come together to place Mtr4 in a 'closed-arch' conformation. This contrasts the dramatically open conformation of the arch in Mtr4-exosome complexes (17,18). While the relationship between arch conformation and Mtr4 function are not completely understood, it is worth reiterating that we are monitoring initial RNA recognition events while the exosome-bound structures represent later states following translocation and delivery of the RNA to the exosome.

It seems likely that arch function in Mtr4 RNA binding and unwinding is regulated by Mtr4 interacting partners in complexes such as TRAMP. Whether and how these complexes exploit any of the intrinsic substrate selectivity mechanisms of Mtr4 remains to be seen. We note that Mtr4 recruitment by ribosome processing factors is mediated through protein–protein interactions in the fist via the arch interacting motifs of Nop53, Utp18 and NVL (35,36). The N-terminus of Air2 (a component of TRAMP) also binds to this same region (37). Future studies are needed to better understand the interplay between RNA, Mtr4 and

Mtr4-interacting proteins. The application of HDX offers a promising path forward to characterization of this dynamic system.

SUPPLEMENTARY DATA

Supplementary Data are available at NAR Online.

ACKNOWLEDGEMENTS

We thank members of the D'Arcy and Johnson Groups for critical discussions.

FUNDING

REFERENCES

1. Chlebowski,A., Lubas,M., Jensen,T.H. and Dziembowski,A. (2013) RNA decay machines: the exosome. *Biochim. Biophys. Acta (BBA) - Gene Regul. Mech.*, **1829**, 552–560.
2. Januszyk,K. and Lima,C.D. (2014) The eukaryotic RNA exosome. *Curr. Opin. Struct. Biol.*, **24**, 132–140.
3. Schmid,M. and Jensen,T.H. (2019) The nuclear RNA exosome and its cofactors. *Adv. Exp. Med. Biol.*, **1203**, 113–132.
4. Schneider,C. and Tollervey,D. (2013) Threading the barrel of the RNA exosome. *Trends Biochem. Sci*, **38**, 485–493.
5. Staals,R.H.J. and Pruijn,G.J.M. (2010) The human exosome and disease. *Adv. Exp. Med. Biol.*, **702**, 132–142.
6. Laffleur,B. and Basu,U. (2019) Biology of RNA surveillance in development and disease. *Trends Cell Biol.*, **29**, 428–445.
7. Fabre,A. and Badens,C. (2014) Human mendelian diseases related to abnormalities of the RNA exosome or its cofactors. *Intractable Rare Dis. Res.*, **3**, 8–11.
8. Olsen,K.J. and Johnson,S.J. (2021) Mtr4 RNA helicase structures and interactions. *Biol. Chem.*, **402**, 605–616.
9. Weick,E.M. and Lima,C.D. (2021) RNA helicases are hubs that orchestrate exosome-dependent 3′–5′ decay. *Curr. Opin. Struct. Biol.*, **67**, 86–94.
10. Delan-Forino,C., Schneider,C. and Tollervey,D. (2017) Transcriptome-wide analysis of alternative routes for RNA substrates into the exosome complex. *PLos Genet.*, **13**, e1006699.
11. Bernstein,J., Ballin,J.D., Patterson,D.N., Wilson,G.M. and Toth,E.A. (2010) Unique properties of the mtr4p−poly(a) complex suggest a role in substrate targeting. *Biochemistry*, **49**, 10357–10370.
12. Jia,H., Wang,X., Anderson,J.T. and Jankowsky,E. (2012) RNA unwinding by the trf4/air2/mtr4 polyadenylation (TRAMP) complex. *Proc. Nat. Acad. Sci. USA*, **109**, 7292–7297.
13. Liang,S., Hitomi,M., Hu,Y.H., Liu,Y. and Tartakoff,A.M. (1996) A DEAD-box-family protein is required for nucleocytoplasmic transport of yeast mRNA. *Mol. Cell. Biol.*, **16**, 5139–5146.
14. Bernstein,J., Patterson,D.N., Wilson,G.M. and Toth,E.A. (2008) Characterization of the essential activities of saccharomyces cerevisiae mtr4p, a 3′→5′ helicase partner of the nuclear exosome. *J. Biol. Chem.*, **283**, 4930–4942.
15. Wang,X., Jia,H., Jankowsky,E. and Anderson,J.T. (2008) Degradation of hypomodified tRNAiMet in vivo involves RNA-dependent ATPase activity of the DExH helicase mtr4p. *RNA*, **14**, 107–116.
16. Weir,J.R., Bonneau,F., Hentschel,J. and Conti,E. (2010) Structural analysis reveals the characteristic features of mtr4, a DExH helicase involved in nuclear RNA processing and surveillance. *Proc. Nat. Acad. Sci. USA*, **107**, 12139–12144.
17. Schuller,J.M., Falk,S., Fromm,L., Hurt,E. and Conti,E. (2018) Structure of the nuclear exosome captured on a maturing preribosome. *Science (New York, N. Y.)*, **360**, 219–222.
18. Weick,E.-M., Puno,M.R., Januszyk,K., Zinder,J.C., DiMattia,M.A. and Lima,C.D. (2018) Helicase-Dependent RNA decay illuminated by a Cryo-EM structure of a human nuclear RNA exosome-mtr4 complex. *Cell*, **173**, 1663–1677.
19. Jankowsky,E. and Fairman-Williams,M.E. (2010) An introduction to RNA helicases: superfamilies, families, and major themes. In: Jankowsky,E. (ed). *RNA Helicases*. The Royal Society of Chemistry Publishing, pp.1–31.
20. Taylor,L.L., Jackson,R.N., Rexhepaj,M., King,A.K., Lott,L.K., van Hoof,A. and Johnson,S.J. (2014) The mtr4 ratchet helix and arch domain both function to promote RNA unwinding. *Nucleic Acids Res.*, **42**, 13861–13872.
21. Halbach,F., Rode,M. and Conti,E. (2012) The crystal structure of s. cerevisiae ski2, a DExH helicase associated with the cytoplasmic functions of the exosome. *RNA*, **18**, 124–134.
22. Johnson,S.J. and Jackson,R.N. (2013) Ski2-like RNA helicase structures: common themes and complex assemblies. *RNA Biol.*, **10**, 33–43.
23. Falk,S., Tants,J.-N., Basquin,J., Thoms,M., Hurt,E., Sattler,M. and Conti,E. (2017) Structural insights into the interaction of the nuclear exosome helicase mtr4 with the preribosomal protein nop53. *RNA*, **23**, 1780–1787.
24. Studier,F.W. (2005) Protein production by auto-induction in high-density shaking cultures. *Protein Expres. Purif.*, **41**, 207–234.
25. Jackson,R.N., Klauer,A.A., Hintze,B.J., Robinson,H., van Hoof,A. and Johnson,S.J. (2010) The crystal structure of mtr4 reveals a novel arch domain required for rRNA processing. *EMBO J.*, **29**, 2205–2216.
26. Easton,L.E., Shibata,Y. and Lukavsky,P.J. (2010) Rapid, nondenaturing RNA purification using weak anion-exchange fast performance liquid chromatography. *RNA*, **16**, 647–653.
27. Zhang,N., Yu,X., Zhang,X. and D'Arcy,S. (2021) HD-eXplosion: visualization of hydrogen–deuterium exchange data as chiclet and volcano plots with statistical filtering. *Bioinformatics*, **37**, 1926–1927.
28. Morales,Y., Olsen,K.J., Bulcher,J.M. and Johnson,S.J. (2018) Structure of frequency-interacting RNA helicase from neurospora crassa reveals high flexibility in a domain critical for circadian rhythm and RNA surveillance. *PLoS One*, **13**, e0196642.
29. Wang,J., Chen,J., Wu,G., Zhang,H., Du,X., Chen,S., Zhang,L., Wang,K., Fan,J., Gao,S. *et al.* (2019) NRDE2 negatively regulates exosome functions by inhibiting MTR4 recruitment and exosome interaction. *Genes Dev.*, **33**,536–549.
30. Conrad,K.S., Hurley,J.M., Widom,J., Ringelberg,C.S., Loros,J.J., Dunlap,J.C. and Crane,B.R. (2016) Structure of the frequency-interacting <scp>RNA</scp>helicase: a protein interaction hub for the circadian clock. *EMBO J.*, **35**, 1707–1719.
31. Büttner,K., Nehring,S. and Hopfner,K.-P. (2007) Structural basis for DNA duplex separation by a superfamily-2 helicase. *Nat. Struct. Mol. Biol.*, **14**, 647–652.
32. Jia,H., Wang,X., Liu,F., Guenther,U.-P., Srinivasan,S., Anderson,J.T. and Jankowsky,E. (2011) The RNA helicase mtr4p modulates polyadenylation in the TRAMP complex. *Cell*, **145**, 890–901.
33. Hageman,T.S. and Weis,D.D. (2019) Reliable identification of significant differences in differential hydrogen exchange-mass spectrometry measurements using a hybrid significance testing approach. *Anal. Chem.*, **91**, 8008–8016.
34. Patrick,E.M., Srinivasan,S., Jankowsky,E. and Comstock,M.J. (2016) The RNA helicase mtr4p is a duplex-sensing translocase. *Nat. Chem. Biol.*, **13**, 99–104.
35. Lingaraju,M., Johnsen,D., Schlundt,A., Langer,L.M., Basquin,J., Sattler,M., Heick Jensen,T., Falk,S. and Conti,E. (2019) The MTR4 helicase recruits nuclear adaptors of the human RNA exosome using distinct arch-interacting motifs. *Nat. Commun.*, **10**, 3393.
36. Du,Y., An,W., Zhu,X., Sun,Q., Qi,J. and Ye,K. (2020) Cryo-EM structure of 90S small ribosomal subunit precursors in transition states. *Science*, **369**, 1477–1481.
37. Falk,S., Weir,J.R., Hentschel,J., Reichelt,P., Bonneau,F. and Conti,E. (2014) The molecular architecture of the TRAMP complex reveals the organization and interplay of its two catalytic activities. *Mol. Cell*, **55**, 856–867.